Energy & Environmental Science

ROYAL SOCIETY OF CHEMISTRY

PAPER

View Article Online
View Journal | View Issue

Cite this: *Energy Environ. Sci.*, 2025, **18**, 354

Efficient fully textured perovskite silicon tandems with thermally evaporated hole transporting materials†

Bhushan P. Kore, *[ab] Oussama Er-raji,[ab] Oliver Fischer,[ab] Adrian Callies,[a] Oliver Schultz-Wittmann,[a] Patricia S. C. Schulze,[a] Martin Bivour,[a] Stefaan De Wolf,[c] Stefan W. Glunz[ab] and Juliane Borchert[ab]

Received 28th August 2024,
Accepted 11th November 2024

DOI: 10.1039/d4ee03899a

rsc.li/ees

Fully textured perovskite silicon tandem solar cells effectively minimize reflection losses and are compatible with industrial silicon production lines. To facilitate the scalability and industrial deployment of perovskite silicon tandems, all functional layers, including the perovskite layer, must be deposited with scalable techniques. Currently, self-assembling molecules (SAMs), polymeric and low-molecular-weight organic semiconductors, are widely used as hole transport layers (HTLs) in p–i–n structured perovskite solar cells. Usually, SAMs are deposited using the spin coating method, but the use of this method could be challenging with large area textured silicon substrates, leading to inhomogeneous SAM layers and lossy HTL/perovskite interfaces. To address this issue, we investigated thermal evaporation of SAMs (2PACz and Me-4PACz) and some other HTLs, such as TaTm and Spiro-TTB. We examined the effect of varying HTL thicknesses on device performance and showed that the thickness of the thermally evaporated HTLs significantly affects the open circuit voltage (V_{OC}) and fill factor (FF) of solar cells. Furthermore, using ultraviolet photoemission spectroscopy and *Suns*-V_{OC} measurements, we correlated the changes observed in the V_{OC} and FF with HTL thickness variations to changes in energy band positions (loss in hole selectivity) and effective resistance losses, respectively. With the optimized HTL thickness, we obtained ~30% efficiency in 1 cm^2 area and ~26% in 4 cm^2 area tandem devices.

Broader context

Fully textured perovskite silicon tandem solar cells have emerged as a highly promising technology for widespread deployment. However, a significant challenge to their commercialization is the development of scalable methods for depositing perovskite and functional layers. Although hybrid processing techniques have shown promise for scalable perovskite deposition with impressive efficiency, extending these results to large-area devices requires scalable processes for all functional layers. Self-assembled monolayers (SAMs) are widely used as hole transport layers (HTLs) in perovskite solar cells owing to their ability to form high-quality, low-loss interfaces with the perovskite. However, conventional spin-coating methods for SAM deposition face difficulties when applied to large-area, textured silicon substrates. To overcome these difficulties, our study investigates the use of thermal evaporation as an alternative method for HTL deposition. We found that the thickness of thermally evaporated HTLs significantly affects device performance, particularly open circuit voltage (V_{OC}) and the fill factor (FF). By optimizing HTL thickness, we were able to achieve high efficiencies in fully textured perovskite-silicon tandem devices. This work presents a scalable and efficient process for HTL deposition, offering a viable solution for the fabrication of large-area, fully textured tandem solar cells without sacrificing efficiency.

1. Introduction

Perovskite silicon tandem solar cells have gained significant attention and shown significant progress in the last few years in terms of improvements in device efficiency.[1–3] Recently, efficiencies well beyond the theoretical single-junction limit (29.4%) of silicon (considering Auger recombination) have been reported in perovskite silicon tandem solar cells.[4–6] These high-efficiency perovskite silicon tandem solar cells often use planar

[a] *Fraunhofer Institute for Solar Energy Systems ISE, Heidenhofstr. 2, 79110 Freiburg, Germany. E-mail: bhushan.kore@ise.fraunhofer.de*
[b] *Chair of Photovoltaic Energy Conversion, Department of Sustainable Systems Engineering (INATECH), University of Freiburg, Emmy-Noether-Strasse 2, 79110 Freiburg, Germany*
[c] *Division of Physical Science and Engineering (PSE), King Abdullah University of Science and Technology (KAUST), Thuwal 23955-6900, Kingdom of Saudi Arabia*

† Electronic supplementary information (ESI) available. See DOI: https://doi.org/10.1039/d4ee03899a

(polished) front[1] or nano/sub-micron textured front[7,8] and textured back silicon wafers/bottom solar cells where the top perovskite layer and other functional layers are usually processed *via* the solution processing route. Theoretical simulations suggest that a planar front design leads to higher reflection losses due to the reflective front surface, resulting in tandem devices with lower short-circuit current densities (j_{SC}).[9–11] In fully textured configuration, a silicon wafer has μm-sized pyramids textured on both sides,[12] used in industrial production of silicon solar cells. In this type of configuration, to guarantee full and conformal coverage, an attractive approach consists of depositing the perovskite through a combination of solution and vacuum deposition techniques, usually referred to as a 'hybrid route'. Here, a porous layer of PbI_2 + CsX (X = I or Br), also called a scaffold, is thermally evaporated onto a textured silicon substrate, followed by infiltration of organic salts *via* spin-coating and thermal annealing to form a polycrystalline perovskite layer. As a result, the deposited perovskite conformally covers the pyramids, adhering to the morphology of the silicon texture.[12] The presence of a pyramidal texture at the front aids the interaction of incident light with the textured surface, which lowers reflection losses and maximizes light absorption.[9,13,14] This further boosts the overall efficiency and energy yield of tandem devices and enables compatibility with industrial silicon production lines.

Initially, different hole transporting layers (HTLs), such as poly-triarylamine (PTAA), poly(3,4-ethylenedioxythiophene): polystyrene sulphonate (PEDOT:PSS), poly-TPD, and NiO_x, have been employed in p–i–n structured perovskite solar cells.[15–17] These HTLs are not ideal because they have several drawbacks. PTAA and poly-TPD suffer from poor surface wettability,[18] temperature and moisture-induced degradation[19] require doping and/or interface modification to achieve higher open circuit voltage (V_{OC}) and better wettability.[18,20,21] PEDOT, commonly used as a hole transport layer, suffers from drawbacks such as its hygroscopic and acidic nature, leading to moisture absorption and device degradation. Additionally, poor energy level alignment and low conductivity hamper the device performance.[15,22–24] Sputtered NiO_x is mostly used as a HTL in fully textured tandems to ensure the conformal coating on the textured surface.[25,26] The problem associated with NiO_x is its surface sensitivity and the necessity of post-surface treatment to passivate the surface, which prevents the interaction of NiO_x with perovskite; otherwise, unwanted complexes are formed at the interface and hamper the device performance (mainly V_{OC}).[25,26] In addition, doping, post annealing treatment and precise control of the reacting gases while sputtering are vital to improve the NiO_x quality and also help in achieving higher V_{OC}.[26–29] Because the recombination losses at the HTL/perovskite interface determine the device's final V_{OC}, choosing the right HTL is crucial, and an ideal HTL must overcome the aforementioned drawbacks. SAM-based HTLs, which were first investigated by Al-Ashouri *et al.*,[30] are now being extensively used in the perovskite community due to their exceptional abilities.[1,2,4,7] Compared to the other HTLs, such as PTAA and PEDOT:PSS, SAM-based HTLs offer efficient extraction of charge carriers, better hole selectivity and lower non-radiative recombination at the HTL/perovskite interface. These properties make SAM-based HTLs ideal for tandem devices, achieving record high power conversion efficiencies (PCEs) in monolithic tandem devices.[1,2,4]

Spin coating is primarily used to deposit SAMs.[30] However, achieving a uniform layer on a large textured surface presents a significant challenge.[31–33] Specifically, the thickness of the SAM layer can vary from the tip of the pyramid to the valleys, resulting in non-uniform coverage. This issue becomes more pronounced with the use of larger pyramid textures, making it difficult to produce homogeneous depositions of these ultrathin SAM layers. Besides, the surface functionality and microstructure of the transparent conductive oxide (TCO) significantly influence the self-assembly of the spin-coated SAMs, as SAM adsorption is highly sensitive to the complex surface chemistry of the oxide.[2,34,35] Additionally, static spin-coating of SAMs with dwell time (time between dropping the SAM solution on the static substrate until the start of the spin coating) of 1 sec to 60 sec, which is usually monitored manually, introduces additional uncertainty during processing and has a strong influence on device performance.[36,37] The spin-coating of HTLs and organic salts in the second step of the hybrid route are the two main obstacles to scaling up the fabrication. To obtain more reliable results and scale up the production of perovskite silicon tandems, an alternative scalable technique is required. Recently, Farag *et al.* successfully demonstrated the thermal evaporation of several SAMs (2PACz, MeO-2PACz, and Me-4PACz) for planar, single-junction perovskite solar cells.[38] They did not observe any chemical differences between the evaporated SAMs compared to their solution-processed counterparts; as a result, comparable device performance was obtained. Apart from this study, no further investigations have been conducted with evaporated SAMs. Furthermore, as perovskite silicon tandem solar cell technology approaches closer to commercialization, scalable processes for the deposition of all functional layers in the tandem device are highly desirable for the production of efficient large area tandem devices. Thus, the thermal evaporation of HTLs offers a scalable method for depositing various types of HTLs on both lab scale (small area, 1 cm^2) as well as full wafer size tandem devices.

The thickness of the SAM layer when deposited *via* the solution processing technique is under debate in the literature with regard to the formation of the ultrathin monolayer of SAMs. It is presumed that when SAMs are deposited using the wet chemical technique, they form a self-assembled monolayer (a single, closely packed layer of molecules) by forming a covalent bond with the TCO.[30] Despite the extensive use of SAMs and other HTLs, such as TaTm and Spiro-TTB in perovskite silicon tandems, the impacts of the thickness variation of these HTLs on energy band alignment, loss of hole selectivity, and series resistance losses are rarely investigated. In the present work, we successfully employed the thermal evaporation of different HTLs (TaTm, Spiro-TTB, 2PACz, and Me-4PACz) and systematically studied the impact of variations in the thickness of HTLs on device performance. We obtained similar tandem device performance for spin-coated and evaporated 2PACz. We observe that the HTL

layer thickness has a significant influence on the device's performance, particularly on the fill factor (FF) and V_{OC}, which makes the HTL thickness crucial for achieving high-efficiency tandems. In addition, we studied whether the underlying HTL has any impact on the formation of the evaporated scaffold and, consequently, the quality of the perovskite. Evaporated HTLs with optimized evaporation rates and thickness enabled us to achieve PCEs close to 30% in fully textured tandem devices. This study presents the use of thermally evaporated HTLs in a fully textured solar cell configuration to help this technology advance a step closer to commercialization.

2. Results and discussion

2.1. Evaporation of hole transporting layers and their morphological and optical characterizations

Fig. 1a illustrates the chemical structures of the different HTLs, such as 2PACz ([2-(9*H*-carbazol-9-yl)ethyl]phosphonic acid), TaTm (*N*4,*N*4,*N*4′,*N*4′-tetra([1,1′-biphenyl]-4-yl)-[1,1′:4′,1′-terphenyl]-4,4′-diamine), Spiro-TTB (2,2',7,7'-tetra(*N*,*N*-di-*p*-tolyl)amino-9,9-spirobifluorene) and Me-4PACz ((4-(3,6-dimethyl-9*H*-carbazol-9-yl)butyl)phosphonic acid). Among these HTLs, SAMs (2PACz and Me-4PACz) in particular are typically coated on oxide or ITO surfaces with either dip coating or spin coating technique,[30] followed by annealing to reinforce the bonding between organic phosphonic acids with the ITO surface. However, in the case of Spiro-TTB and TaTm, there is no bond formation between the ITO surface and HTL, so evaporated Spiro-TTB and TaTm are usually used without any post annealing treatments.[39,40] We demonstrated the thermal evaporation of SAMs and other HTLs on textured silicon solar cells, followed by top cell perovskite processing *via* the hybrid route. The thermally evaporated HTLs were used as evaporated without any post annealing treatment. The cross sectional scanning electron microscopy (SEM) images, shown in Fig. 1b, demonstrate the conformal coating of the thermally evaporated TaTm layer on a textured pyramid substrate with textured silicon/ITO/TaTm stack. The top and cross sectional view SEM images of thermally evaporated HTL films on planar Si substrates (Fig. S1, ESI†) show the formation of a compact layer.

The transmittance and absorptance spectra of all HTLs (deposited on glass substrate) used in this study with the optimized thickness from the *jV* measurements are shown in Fig. 1c for comparison. A systematic variation in the transmittance and absorptance spectra was observed with an increase in the thickness of HTL (Fig. S2 and S3, ESI†) both on glass/HTL and glass/ITO/HTL stacks. In the case of TaTm and Spiro-TTB, a gradual increase (decrease) in the absorptance (transmittance) can be observed with an increase in the thickness of the HTL layer. However, in the case of SAMs, there is barely any change in the transmittance and absorptance spectra even after increasing the thickness to 7 nm, indicating that a thick layer of SAMs is also transparent to visible light because the transmittance and absorptance spectra of spin-coated SAMs and thermally evaporated SAMs are almost identical. Fig. 1d and e show a comparison of AFM images of spin-coated and thermally evaporated 2PACz. As highlighted in the case of spin-coated 2PACz, some agglomerates on the surface may originate from 2PACz molecules that are not bonded to the ITO surface, as predicted by molecular dynamic simulations.[36] In contrast, the surface of the evaporated 2PACz appears to be smooth and homogeneous without any apparent agglomerates. All the evaporated HTLs exhibit smooth surface morphology

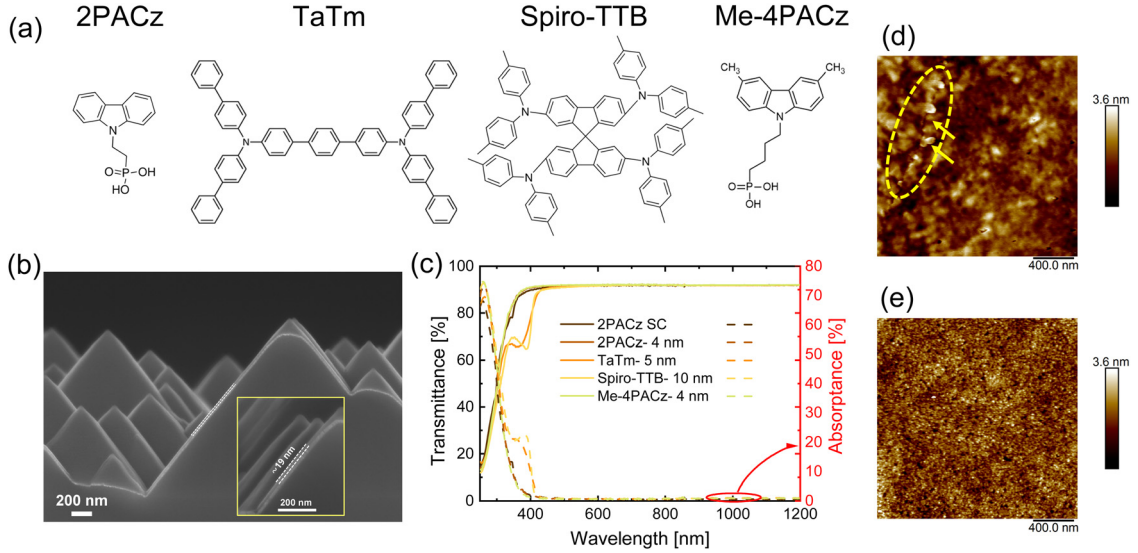

Fig. 1 (a) Chemical structures of 2PACz, TaTm, Spiro-TTB and Me-4PACz. (b) SEM image of a 20 nm thick thermally evaporated TaTm layer on a textured Si substrate with a textured silicon/ITO/TaTm stack. (c) Transmittance and absorptance spectra of different thermally evaporated HTLs deposited on a bare glass substrate compared with the spin-coated 2PACz (2PACz SC) used as a reference HTL in this work. The thickness of different HTLs is given for textured substrates and the actual thickness of HTLs on planar substrates is higher, as discussed in the experimental section. Atomic force microscopy (AFM) measurements of planar silicon/ITO/HTL stacks of (d) spin-coated 2PACz (7 mmol) and (e) evaporated 2PACz (4 nm).

without any inhomogeneities, as shown in Fig. S4 (ESI†), with similar root mean square (RMS) surface roughness.

2.2. Perovskite film formation, structural, and optoelectronic properties

We then analysed the formation of a evaporated PbI_2 + CsI scaffold (~550 nm thick) using cross-sectional SEM on different thermally evaporated HTLs (Fig. S5, ESI†). From the cross-sectional SEM images, it is quite evident that the formation of the scaffold (grains, porosity and thickness) is barely influenced due to the presence of different HTLs underneath. The organohalide salt solution of FAI and FABr (FA: formamidinium) with urea as an additive (3 mg mL^{-1}) dissolved in ethanol was spin coated on the inorganic scaffold, followed by annealing at 100 °C to obtain the perovskite films on textured silicon substrates.[41] The X-ray diffraction (XRD) patterns of perovskite ($FA_{0.85}Cs_{0.15}Pb(I_{0.78}Br_{0.22})_3$) with textured silicon/ITO/HTL/perovskite stack are shown in Fig. 2a. The XRD patterns of perovskite processed on different HTLs look almost identical, except for the fact that there is more remnant PbI_2 in the case of spin-coated 2PACz, as highlighted in Fig. 2b, indicating that the conversion of the scaffold into perovskite is better in the case of evaporated HTLs in comparison to spin-coated 2PACz. Furthermore, we investigated the influence of HTL thickness on the perovskite formation; again, we did not observe any noticeable changes in the XRD patterns (Fig. S6, ESI†) irrespective of the evaporated HTLs used. However, in the case of perovskite processed on spin-coated 2PACz, the presence of remnant PbI_2

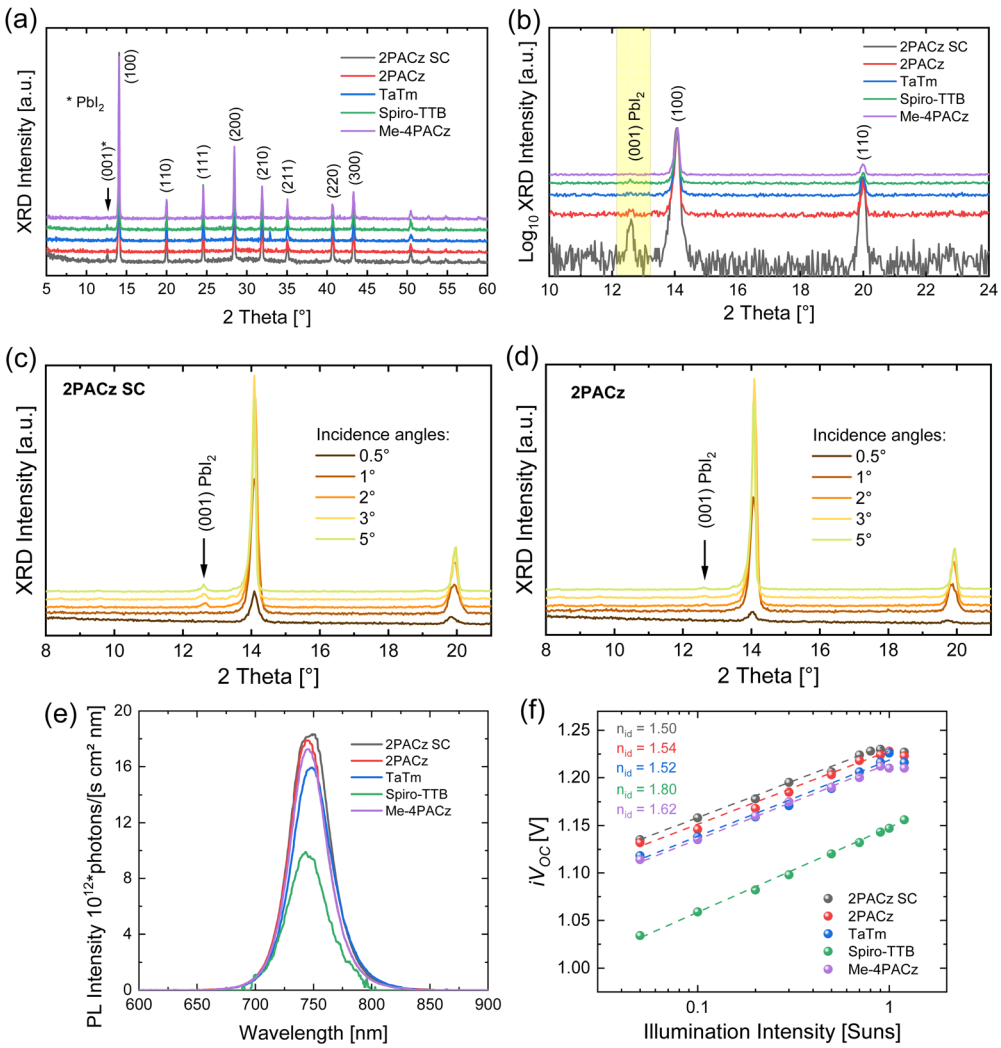

Fig. 2 X-ray diffraction (XRD) patterns of the $FA_{0.85}Cs_{0.15}Pb(I_{0.78}Br_{0.22})_3$ perovskite processed on textured substrates (textured silicon/ITO/HTL/perovskite) with (a) different HTLs, (b) logarithmic scale XRD intensities illustrating the impact of the underlying HTL on the perovskite by comparing the diffraction peak of unconverted PbI_2 (001) impurity (at 12.68 2theta), which is also highlighted in the plot. Grazing-incidence XRD diffractograms of perovskite films with different incident beam angles. The perovskite processed on (c) spin-coated 2PACz and (d) thermally evaporated 2PACz with textured silicon/ITO/2PACz/perovskite configuration. (e) Comparison of steady state photoluminescence (PL) of the perovskite layer processed on different HTLs. (f) Illumination intensity-dependent steady-state photoluminescence quantum yield (PLQY) plot showing variation in the implied V_{OC} (iV_{OC}) (also referred to as quasi Fermi level splitting, QFLS) as a function of incident laser light intensity and ideality factor (n_{id}) extracted from a fit to the intensity-dependent iV_{OC}.

was apparent and reproducible in multiple batches. The remnant PbI_2 at the HTL/perovskite interface can cause unwanted hysteresis in the *jV* curves.[41,42]

We further analysed whether the presence of underlying HTL can influence the formation and hence the overall quality of the perovskite. First, we considered the contact angle of a water droplet on different HTL with glass/ITO/HTL stack, (Fig. S7, ESI†). The contact angle was found to be significantly higher for Spiro-TTB (99°) and TaTm (91°) compared to spin-coated and evaporated SAMs (ranging from 54° to 66°), indicating more hydrophobic surface properties for Spiro-TTB and TaTm. The hydrophobic surface of the HTLs favours the crystallization and orientation of the perovskite film when the perovskite is processed *via* co-evaporation or a wet chemical route.[39,40,43] However, when the perovskite is processed *via* a hybrid route, we do not observe any significant impact of hydrophobicity on the scaffold or the crystallinity of the perovskite film.

In addition, we examine the quality of the perovskite by analyzing the cross-section between HTL and perovskite through SEM to investigate the amount of PbI_2 remaining (bright clusters, typically present at valleys) at the interface between HTL and perovskite (Figure S8, ESI†). We did not observe any striking differences in the presence of PbI_2 at the interface and overall quality of the perovskite layer when the perovskite was processed on evaporated HTLs in comparison to spin-coated 2PACz. Quantifying remnant PbI_2 amount based on cross sectional SEM measurements could be misleading as the percentage of unconverted PbI_2 can vary from one spot to another, which makes the analysis difficult.

Furthermore, to obtain more bulk sensitive and in-depth information, we carried out grazing-incidence XRD measurements on perovskite layers. In comparison to standard Bragg–Brentano geometry, GI-XRD facilitates more depth-dependent information about the perovskite's composition by increasing the incidence angle θ. A higher incidence angle probes more into the depth of the perovskite; hence, by increasing this angle, one can obtain more information about the HTL/perovskite interface, which is buried by a thick perovskite layer. As shown in Fig. 2c and d, in the case of spin-coated 2PACz, we observe a diffraction peak corresponding to PbI_2 emerging as the incident angle increases. However, with evaporated 2PACz, this peak is less prominent. A similar conclusion can be drawn for the other thermally evaporated HTLs (Fig. S9, ESI†). Hence, it is quite obvious from the XRD analysis that the conversion of the scaffold into perovskite is improved when thermally evaporated HTLs are present underneath the scaffold, which could be related to the formation of homogeneous or more compact HTL by thermal evaporation compared to spin coating.

Next, we examined the non-radiative recombination at the HTL/perovskite interface for different HTLs. We perform steady state photoluminescence (PL) measurements on perovskite films to extract the PL quantum yields and internal implied V_{OC} (iV_{OC}) or quasi Fermi level splitting (QFLS) of the perovskite (Fig. 2e and Fig. S10, S11, ESI†). The iV_{OC} values for the thin layers of evaporated HTLs, measured at ~1 sun illumination, were found to be significantly lower compared to the spin-coated 2PACz reference, which then improved after increasing the thickness, and almost similar iV_{OC} values were obtained for evaporated HTLs except in the case of Spiro-TTB. The lower iV_{OC} values for very thin layers of HTLs can be attributed to the formation of non-homogeneous HTL films, allowing for direct contact between the underlying ITO and perovskite, hence resulting in severe non-radiative recombination losses. The steady state PL plots shown in Fig. S11 (ESI†) also support this observation. However, for Spiro-TTB, significantly lower iV_{OC} values were obtained irrespective of the thickness of the layer, indicating more non-radiative losses/surface recombination losses at the Spiro-TTB/perovskite interface. Overall, intense PL peaks (Fig. 2e) were obtained by employing different HTLs (with optimized thickness), without much shift in the PL peak position, suggesting the formation of high quality polycrystalline perovskite.

The internal ideality factor (n_{id}), which provides information about the dominant recombination type in perovskite, was obtained from light intensity-dependent iV_{OC} measurements, as shown in Fig. 2f. The ideality factor is quite comparable for spin-coated 2PACz and evaporated 2PACz, and it is found to be close to 1.5, indicating a predominant radiative and reduced trap-assisted Shockley–Read Hall recombination.[44] However, n_{id} values show strong deviation, especially for Spiro-TTB predicting more recombination losses and hence lower V_{OC} in Spiro-TTB-based devices.

To gain more insight into the charge carrier dynamics, time-resolved photoluminescence (TRPL) measurements (Fig. S12, ESI†) were performed. The TRPL results further corroborate the trend observed in iV_{OC}, *i.e.* very low carrier lifetime for very thin layers of HTL. The carrier lifetime improves by further increasing the thickness of the HTLs. The carrier lifetime is comparable for spin-coated and evaporated 2PACz. The decay curves for TaTm and Spiro-TTB were fitted with bi-exponential decay functions, each with different carrier lifetimes, indicating two different types of recombination pathways in the perovskite, as shown in Fig. S12 (ESI†). The shorter decay component is usually associated with non-radiative recombination. This is often caused by surface defects, trap states, or recombination at grain boundaries.[45,46] The longer decay component represents radiative recombination, where charge carriers recombine within the bulk of the material, emitting photons. In our study, the dominance of a shorter decay lifetime for thin HTL layers reflects more surface or interface losses. In contrast, the longer lifetime improves as the HTL thickness increases, indicating the presence of fewer defects or improved material quality. Longer lifetimes are typically observed in efficient perovskite materials, where carriers diffuse more effectively through the bulk before recombination.[6,46] Overall, based on the structural and optoelectronic characterizations, it can be concluded that the quality of perovskite with evaporated 2PACz is similar to spin-coated 2PACz, with some additional improvements. The other HTLs, such as TaTm, also exhibit good structural and optoelectronic quality of the perovskite compared to the evaporated 2PACz. Perovskite deposited on the evaporated

TaTm and 2PACz exhibits similar structural and optoelectronic properties.

2.3. Effect of thickness variation of the TaTm layer on the tandem solar cell performance

To compare the performance of tandem devices, we fabricated fully textured p–i–n perovskite solar cells on top of the silicon heterojunction bottom cell with different thermally evaporated HTLs and compared the solar cell performance with the spin-coated 2PACz reference (2PACz SC). The schematic of the device layout is shown in Fig. 3a. A case study of TaTm as a HTL and corresponding *jV* data of the tandem devices with TaTm thickness varying from 2 nm to 20 nm are shown in Fig. 3b. The thickness of the TaTm layer barely affects the j_{SC} of the tandem devices, as a small drop in j_{SC} was observed with an increase in the thickness. The V_{OC} of the devices is strongly affected by the thickness of the TaTm layer. Lower V_{OC} values were obtained for the 2 nm thick TaTm layer, which further improved for the 5 nm thick TaTm layer. This is also corroborated by the iV_{OC} results discussed in the previous section. The V_{OC} values obtained with TaTm as the HTL are comparable to the V_{OC} of the reference devices. A further increase in the thickness results in a strong drop in V_{OC}. A nearly similar trend was also observed in the FF. Consequently, we obtain the highest possible efficiencies (~27%) for the 5 nm thick TaTm layer.

The V_{OC} of the reference devices shows a large spread compared to devices with evaporated TaTm, again illustrating the advantage of using thermally evaporated HTLs, especially in a fully textured tandem configuration. Conformal coating of micro-meter-sized textured pyramids with an ultrathin layer of spin-coated 2PACz is challenging, and the noncovered region can lead to shunting paths, which hampers the device performance and lowers the yield, as discussed in earlier studies.[12,25,28] The other explanation for the observed spread in the *jV* data could be related to the presence of unbonded phosphonic acid molecules on the top of the monolayer because we did not wash the 2PACz layer after spin coating.[47]

To further understand and confirm the trend observed in V_{OC} and FF, we fabricated single junction perovskite solar cells on top of the ohmic textured silicon substrates, (Fig. S13, ESI†). An almost identical trend of variation in V_{OC} and FF is observed, indicating that the trend in tandem devices is

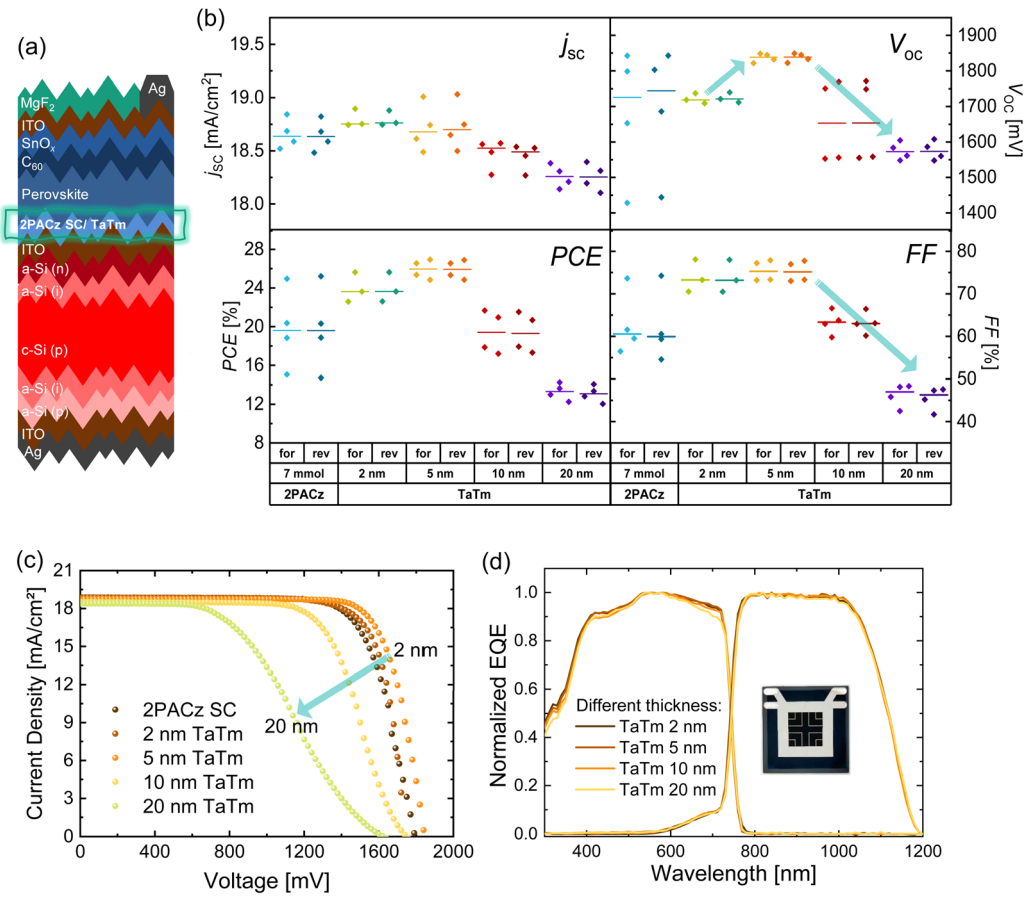

Fig. 3 (a) Schematic of a fully textured perovskite silicon tandem solar cell architecture. (b) Variation in the *jV* parameters (j_{SC}, V_{OC}, FF and PCE) of the tandem devices with an increase in the thickness of the TaTm layer from 2 nm to 20 nm. All the tandem devices have an active area of 1 cm^2, unless otherwise mentioned. The tandem device performance was also compared with spin-coated 2PACz (2PACz SC) as a HTL. (c) *jV* curves of the best performing solar cells from each group scanned at a scan rate of 34 mV s^{-1} in the reverse direction (V_{OC} to j_{SC}). (d) Normalized EQE of tandem solar cells for different thicknesses of TaTm, and inset showing the photo of the tandem solar cell.

reproducible. The shape of the *jV* curves of both the single junction (Fig. S13c, ESI†) and tandem (Fig. 3c) devices shows a strong change in the shape of the *jV* curves and hence the performance of the devices with an increase in the TaTm thickness. These findings are similar to the results obtained by Susic *et al.*[40] Although in EQE of the single junction (Fig. S13b, ESI†) or tandem devices (Fig. 3d), we did not observe any significant change in the shape that could lead to such a drastic change in the shape of the *jV* curves. The extracted effective resistance (R_S, series resistance and other resistive contributions) from the slope of the *jV* curves near the V_{OC} for the tandem devices (Fig. S14, ESI†). The R_S for the thick (10 and 20 nm) TaTm layer was quite high (80–120 Ω cm^2) compared to the optimized TaTm layer (5–10 Ω cm^2).

It has been reported in the literature that the ohmic contact between ITO and TaTm reduces the FF and PCE of the PSCs, and to overcome this problem, a material with a higher work function (WF), such as metal oxides or organic semiconductors, is usually used as an interlayer between ITO and TaTm.[40,48–50] In our perovskite silicon tandem/single junction perovskite configuration, we did not use an interlayer between ITO and TaTm. Despite this, we achieved an FF of ∼80% in both device configurations.

We carried out similar studies of systematic variation in the thickness of 2PACz and Spiro-TTB (Fig. S15 and S16, ESI†). In the case of evaporated 2PACz, we observed a gradual increase in V_{OC} with an increase in thickness from 0.5 nm to 7 nm, while a significant drop in FF was witnessed for the highest thickness of 2PACz (Fig. S15, ESI†). We found 4 nm thick 2PACz to be optimum for obtaining the highest PCE (∼27%) tandem devices. Furthermore, both spin-coated and evaporated 2PACz deliver similar V_{OC} in the tandem devices. Based on the *jV* results, we can say that in the case of evaporated 2PACz, the covalent bond formation with ITO occurs even without annealing the evaporated 2PACz layer. For comparison, we also provided the *jV* data of tandem cells with varying 2PACz concentrations (Fig. S16, ESI†). The spin-coated 2PACz showed less variation in *jV* parameters with changes in concentration than the evaporated 2PACz, which showed systematic enhancements in V_{OC} and FF with increased layer thickness. This demonstrates that the deposition technique has a significant impact on the formation of the 2PACz layer although the optimized concentration and thickness yield similar device performance. A comparison of the spread in the *jV* data when 2PACz was deposited using two different methods demonstrated the clear advantage of using the thermally evaporated 2PACz. Notably, cells containing 7 mmol of 2PACz showed less spread in the *jV* data likely due to improved layer formation at higher concentrations.

Unlike TaTm and 2PACz, the tandem devices with Spiro-TTB demonstrated the lowest V_{OC} (150 mV lower than spin-coated 2PACz), which was already anticipated from the iV_{OC} results where lower iV_{OC} values were obtained irrespective of the thickness of the layer, but because of higher FF, we were able to obtain almost similar device performance (∼26%) as we obtained for TaTm and 2PACz (Fig. S17, ESI†). Additionally, as reported by Sahli *et al.*, the thermally evaporated Spiro-TTB on top of ITO detaches from the pyramids and accumulates at the valleys during the annealing (150 °C) step used for crystallization of the perovskite.[12] In our study, we did not observe the melting of evaporated Spiro-TTB when annealed at 100 °C (perovskite crystallization temperature). However, at a higher temperature (150 °C), which exceeds the glass transition temperature of Spiro-TTB, we observe an accumulation of melted Spiro-TTB in the valleys (see Fig. S18, ESI†).

2.4. Effect of thickness variation of TaTm layer on the energy band alignment, mismatch between QFLS and V_{OC} and effective resistance analysis of tandem devices

As observed from the *jV* results of the tandem devices, the best V_{OC} was obtained for the 5 nm thick TaTm and 2PACz (spin coated or evaporated) layer. The V_{OC} of the tandem device is sensitive to several factors, such as changes in the energetic alignment, less energy barrier leading to higher hole selectivity, changes in the bulk properties of the perovskite or changes at the interface (HTL/perovskite or perovskite/ETL). The chances of the latter, changes in the bulk properties of the perovskite, are lower, as we observed from the XRD and PL measurements that the perovskite film quality and the optoelectronic properties are not influenced by the underlying HTL. To further support this claim, we extracted the Urbach energy from the slope of the exponential increase in the absorption edge[30,51] and found it to be around 14 ± 2 meV for different HTLs underneath perovskite (Fig. S19, ESI†). The low values of Urbach energy values indicate the lower disorder and better crystalline quality of the perovskite. Additionally, the Urbach energy values are nearly similar irrespective of the HTLs, and this further adds to the conclusion of unchanged/unaltered optoelectronic properties of perovskite with the use of different HTLs. Hence, we can conclude that the bulk perovskite properties are not significantly altered by the HTLs used in this study. To further demonstrate the changes observed in the V_{OC} of the tandem devices having different HTLs with varying thicknesses, we carried out photoelectron spectroscopy measurements in air (PESA) on textured Si/ITO/HTL and textured Si/ITO/HTL/perovskite stacks (Fig. S20, ESI†). Fig. 4a shows a schematic of the energetic alignment of the HTL's highest occupied molecular orbital (HOMO) levels with respect to the valence band maxima (VBM) of the perovskite. Considering the VB onset of the perovskite and the HOMO levels of the different HTLs, it is evident that TaTm, 2PACz and Me-4PACz are energetically more hole selective compared to Spiro-TTB. The energy barrier between the perovskite's VBM and HOMO levels of TaTm, 2PACz and Me-4PACz is smaller in comparison with the VBM of perovskite and HOMO of Spiro-TTB (0.5 eV), which allows for more efficient hole extraction in the case of TaTm and 2PACz, see Table S1 (ESI†). The close alignment of energy levels for 2PACz to the VBM of perovskite leads to higher V_{OC} whereas the large mismatch in the case of Spiro-TTB leads to lower V_{OC}. Furthermore, an increase in the thickness of the TaTm layer from 2 nm to 20 nm leads to a large energy offset of 0.23 eV (2 nm) to 0.19 eV (20 nm) and a relatively lower energy offset of

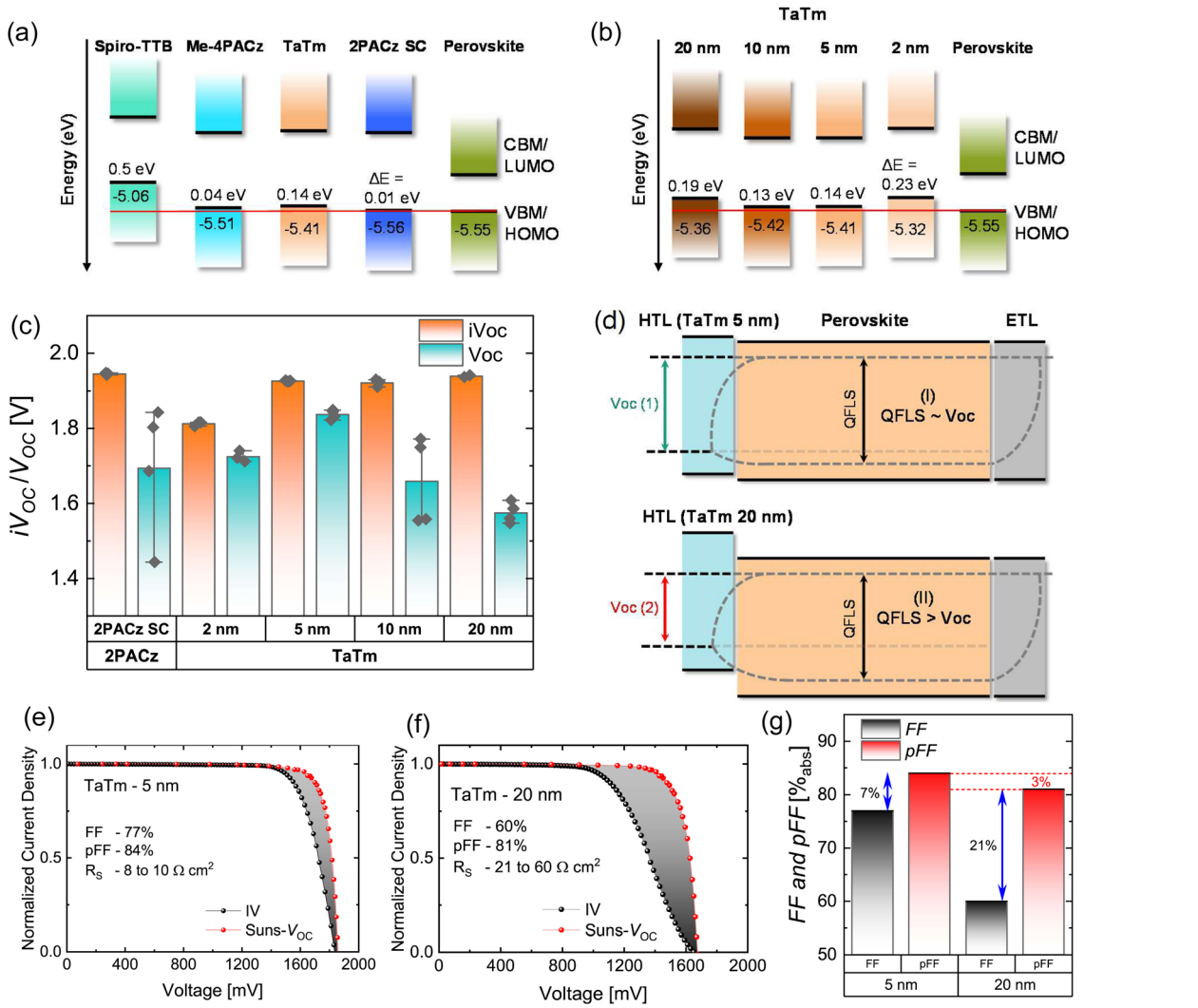

Fig. 4 Energetic alignment and QFLS-V_{OC} mismatch analysis of HTLs and the perovskite/tandem device. (a) Schematic representation of the band edge positions of the different HTLs (with optimized thickness) compared to the perovskite based on PESA measurements. (b) Schematic representation of the valence band edge positions/HOMO of the TaTm layer with an increase in thickness and comparison of energy offset with respect to the VBM of perovskite. (c) Impact of thickness variation in TaTm on QFLS/iV_{OC} (perovskite + silicon) extracted from steady-state PLQY measurements and V_{OC} of the tandem devices extracted from *jV* measurements. For PL measurements, a textured silicon/ITO/HTL/perovskite stack was used, while *jV* measurements were performed on the final tandem device with the device configuration, as shown in Fig. 3a. (d) Schematic representation of changes in the band edge positions of (i) 5 nm and (ii) 20 nm thick TaTm layers in comparison with perovskite illustrating the mismatch between QFLS and V_{OC}. Comparison of *Suns*- V_{OC} and *jV* curves (reverse scan) of textured tandem devices with (e) TaTm – 5 nm and (f) TaTm – 20 nm to achieve effective resistance losses. (g) Comparison of FF and pFF of tandem devices for 5 nm and 20 nm thick TaTm layer.

0.14 eV for a 5 nm thick layer, as shown in Fig. 4b. The large energy offset leads to lower V_{OC} as observed in tandem cells shown in Fig. 3b, as discussed in Subsection 2.3. The change in the thickness of the TaTm layer changes the hole selectivity of the layer quite significantly, which impacts both V_{OC} and FF of the solar cells, as shown previously by Susic *et al.*[40] The study shows a reduced WF of 4.38 for the thicker 10 nm film, suggesting that at this thickness, the surface properties of the material begin to resemble those of its bulk form. As the thickness of the TaTm layer increases, the molecular packing and arrangement may change, affecting the energy levels. Thicker films can lead to altered molecular interactions and stacking, which can influence the energy levels of the valence and conduction bands.

Fig. 4c illustrates the comparison of the QFLS (perovskite + silicon) and V_{OC} of the tandem devices. The trend observed in QFLS with an increase in the TaTm thickness does not complement the trend observed in the V_{OC} of the tandem device. The QFLS of the tandem initially improves and then remains unchanged even for the highest thickness of the TaTm layer, while the V_{OC} of the tandem devices improves for a 5 nm thick TaTm layer and then shows a strong drop with a further increase in the thickness of the TaTm layer. This QFLS/V_{OC} mismatch is also present in the case of 2PACz and Spiro-TTB, as shown in Fig. S21 (ESI†). The QFLS/V_{OC} mismatch can be explained by the energy band alignment between the HTL and perovskite. A schematic of the possible energy band alignment

scheme with TaTm as a HTL with two different thicknesses is given in Fig. 4d. As illustrated in case (i), when the TaTm thickness is 5 nm, this allows the best alignment (0.14 eV) of the HOMO of TaTm to the VBM of perovskite. This results in a very low mismatch between QFLS and iV_{OC}. For case (ii) where the thickness of TaTm is 20 nm, the HOMO of the TaTm layer is significantly shifted upwards (towards vacuum). This leads to a larger energy offset (0.19 eV) between the HOMO of TaTm and the VBM of perovskite. The hole selectivity in the latter case is lower, which significantly lowers the V_{OC}, but this does not lead to a drop in the QFLS because the perovskite is still very well passivated, and the position of the HOMO of the TaTm layer does not influence the QFLS of perovskite, hence resulting in a large mismatch between QFLS and V_{OC}'s.

***Suns*-V_{OC} explanation.** To provide further insight into the variation in FF and R_S with an increase in the thickness of the TaTm layer, we carried out *Suns*-V_{OC} measurements. To estimate the contribution of R_S in the tandem solar cell, we carried out *Suns*-V_{OC} measurements, where the V_{OC} of the cell was measured depending on the illumination intensity. From this measurement, a normalized pseudo *jV* (p*jV*) curve is constructed. This p*jV* curve is free from charge carrier transport losses, which we refer to as effective R_S (series resistance + non-ohmic resistance). Fig. 4e and f show the comparison of *jV* curves measured at a solar simulator and constructed p*jV* curves from *Suns* V_{OC} measurements. The difference between pseudo-FF (pFF) and FF increases with increasing TaTm layer thickness, indicating lower charge carrier extraction efficiencies. From the difference in the voltages from the *jV* and p*jV* curves, a voltage-dependent effective R_S can be extracted. R_S increases from 8 to 10 Ω cm^2 for a 5 nm TaTm layer to 21–60 Ω cm^2 for a 20 nm thick TaTm layer. It is important to note here that the increase in R_S with an increase in TaTm layer thickness is not ohmic because $\Delta V/I$ (voltage difference between *jV* and p*jV* curves near V_{OC}) is spread over a certain range for different currents *I* (as shown in Fig. S22, ESI†). Moreover, the shift in the HOMO of the TaTm layer with an increase in the thickness also influences the R_S values. We also noticed that the increase in the thickness of TaTm from 5 nm to 20 nm significantly increases the difference (pFF–FF) from 7 to 21% and reduces the pFF by 3%, as shown in Fig. 4g. Overall, it can be concluded from this section that a variation in the TaTm layer's thickness leads to changes in the HOMO of the TaTm layer. This, in turn, impacts the V_{OC} of the devices and leads to an increase in effective R_S with an increase in TaTm layer thickness, decreasing the FF of both single junction and tandem devices.

2.5. Best performing tandem cells, actual potential of tandems free from R_S and band alignment losses, and large area tandem cells

To further boost the j_{SC} of the tandem devices, we used a modified metallization mask, as shown in Fig. S23 (ESI†) for Ag evaporation with a silver finger width of ~25 μm. With the use of a U-shaped metallization mask, we were able to reduce the shading due to wider finger widths (~100 μm) in the reference

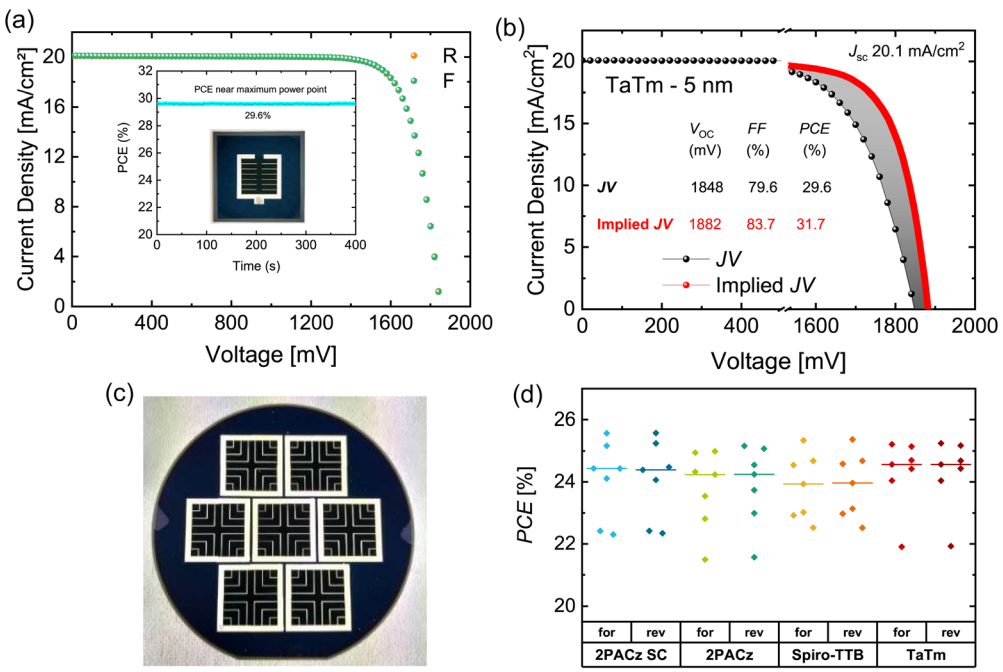

Fig. 5 (a) *jV* curve of the best performing cells with TaTm as the HTL, with new metallization design (shown in the inset) to reduce the shading losses and active area 1 cm^2 and stabilized efficiency of 29.6%. (b) Measured the *jV* curve of the tandem device and reconstructed implied *jV* characteristics of the tandem device from *Suns* PLI measurements. The reconstructed *jV* characteristics show the actual potential of the tandem solar cell, which is free from charge carrier extraction (transport) losses and losses due to the band alignment mismatch at the perovskite/charge transport layer interface. (c) Photograph of the fully processed perovskite silicon tandem device (with TaTm as HTL) on a 4-inch wafer with 7 tandem devices each with a 4 cm^2 active area. (d) PCEs of the tandem devices with different HTLs on a 4 cm^2 active area. The other *jV* parameters are provided in the ESI.† The median (red line) shows average efficiencies beyond 24% for most of the HTLs used in this study.

mask (the metallization used in all the other tandem devices). We obtained an overall gain of about $\sim$1.2 mA cm^{-2} in the j_{SC}. There were also some improvements in the FF ($>$80%) obtained by further optimizing the thickness of the evaporated silver. Using a modified metallization mask with narrow finger widths, we could achieve PCEs of 29.6% in the case of TaTm, as shown in Fig. 5a and Table 1, with a stabilized PCE of 29.6%. This is the highest reported efficiency so far in tandem solar cells with thermally evaporated TaTm as HTL. With other HTLs, we achieved more than 28% PCEs. A summary of the *jV* parameters with all the other HTLs used in this study is tabulated in Table 1. In the case of Me-4PACz, we used the same thickness (4 nm) optimized for evaporated 2PACz. The devices with Me-4PACz delivered $\sim$80 mV lower V_{OC} in tandem devices compared to devices with evaporated 2PACz despite having the lower energy offset between the HOMO of Me-4PACz and the VBM of perovskite, as discussed in Subsection 2.4. Further investigations are underway to understand this discrepancy. We carried out both short-term stability (60 min) under continuous working conditions and long-term stability (210 days) tests on tandem devices with different HTLs. The devices show stable performance under continuous working conditions. The devices retain 90% of the PCEs and show comparable device performance when stored in the dark (N_2 atmosphere) for a longer period, as shown in Fig. S24 (ESI†).

***Suns*-PL Imaging results.** To estimate the actual potential of the tandem solar cell, we carried out contactless *Suns*-PL imaging (*Suns*-PLI). For this implied *jV*, curves are generated by measuring intensity-dependent iV_{OC} images. For each intensity, a PL image of both subcells was recorded, from which the iV_{OC} of the subcells can be calculated following the approach described by Fischer *et al.*,[52] which is averaged over the active area without fingers and busbars. From these mean iV_{OC} values, an implied *jV* curve can be constructed that is scaled to the measured j_{SC}. The implied *jV* curve shows the actual potential of the tandem cell stack which is free from the effective resistance or charge carrier extraction losses and losses due to the energetic mismatch between perovskite and charge transporting layers. The implied *jV* curve for the 5 nm thick TaTm layer and 29.6% PCE (see Fig. 5a and Table 1) suggests the actual potential of the tandem cells to be approximately 2% higher (PCE = 31.7%). This exceeds the PCE of the fully textured tandems reported thus far. Even higher efficiencies can be attained by modifying the top and bottom cell's current mismatch conditions and by further reducing the nonradiative losses at HTL/perovskite and perovskite/ETL interfaces.

Table 1 Summary of the device performances of tandem solar cells (1 cm^2 active area) with different HTLs using a modified metallization mask to achieve higher current densities; all measured in the reverse direction (V_{OC} to j_{SC})

Different HTLs	V_{OC} (mV)	j_{SC} (mA cm^{-2})	FF (%)	PCE (%)
2PACz SC	1876	19.9	76.8	28.7
2PACz	1871	20.0	76.5	28.6
TaTm	1848	20.1	79.6	29.6
Spiro-TTB	1740	19.8	82.6	28.3
Me-4PACz	1790	19.8	79.2	28.0

We further investigated the performance of tandem devices processed on a 4-inch wafer, as shown in Fig. 5c, with an active area of 4 cm^2, to demonstrate the potential of evaporated HTLs on large area tandems. The thickness of the HTLs optimized from the small area tandem devices was used while fabricating the tandem devices on a 4-inch wafer. We obtained more than 24% mean PCE values for the different HTLs used in this study (see Fig. 5d). The lower PCEs on the 4 cm^2 area tandem cells compared to the champion device (29.6%, 1 cm^2) are attributed to lower j_{SC} due to large shading by the metallization mask (with a finger width of $\sim$100 μm) and a small drop in the FF. Higher efficiency and less spread in the *jV* data (see Fig. S25, ESI†) on larger area tandems suggest the potential of thermally evaporated HTLs on even larger areas and higher efficiency tandem devices in the near future.

To further address the discrepancy between TaTm's superior performance in small-area tandem devices and the comparable performance of various HTLs in larger 4 cm^2 devices, we examined our previous results. However, we anticipated a similar performance with 2PACz based on our previous report of higher PCEs using spin-coated 2PACz.[41] In this study, we were unable to replicate those higher PCEs, suggesting that batch-to-batch variation and processing conditions may play a role. We further emphasize that while 30% PCE can be achieved with spin-coated 2PACz, reproducibility remains a challenge, and higher PCEs can be achieved with TaTm and other evaporated HTLs, offering comparable performance to spin-coated HTLs. TaTm likely forms a more homogeneous and robust layer than 2PACz owing to its larger molecular structure, which promotes better surface coverage. In contrast, 2PACz excels during the formation of an ultrathin layer with favorable interface properties but may not match TaTm in terms of mechanical robustness, resulting in more reproducible results with TaTm. The main factor affecting the tandem device performance compared to other *jV* parameters is the FF, and we notice from multiple batches that FF varies significantly in the case of 2APCz compared to TaTm. Overall, the improved device performance in the case of TaTm-based tandems is attributed to more robust layer formation and better reproducibility.

To further improve the V_{OC} and FF of perovskite silicon tandem devices, the bilayer of HTLs can be used, which can help further boost the efficiency of the tandem devices. These will be the topic of future studies, with the aim of establishing efficient and stable interfaces for high PCE tandem solar cells. Considering all the *jV* results with different active area cells, one can conclude that thermally evaporated HTLs deliver reliable results. Additionally, from an upscaling point of view, the thermal evaporation of HTLs offers a scalable option with good spatial uniformity, reproducible device performance, and, most importantly, compatibility with industrially relevant processes.

3. Conclusion

We successfully demonstrated the deposition of thin HTLs on textured substrates by employing the thermal evaporation of

different HTLs otherwise performed *via* solution processing techniques. Based on the structural and optoelectronic characterizations, we confirm that the underlying HTL does not have a substantial influence on the structural and optical properties of the perovskite albeit increasing the thickness of the HTLs causes slight changes in optical properties. Furthermore, the grazing incidence XRD results confirm that evaporated SAMs/HTLs assist in the efficient conversion of the inorganic scaffold into perovskite compared to spin-coated SAMs. The thermally evaporated HTLs deliver similar QFLS and V_{OC} compared to their solution-processed counterparts. The QFLS-V_{OC} mismatch observed with increasing the HTL thickness is attributed to changes in the HOMO of the HTLs, which increases the energy band offset, causing a significant drop in the V_{OC} but without affecting the QFLS. The increase in HTL thickness also enhances the effective R_S, which significantly reduces the FF. Based on the trend observed in V_{OC} and offset between the HOMO levels of different HTLs and VBM of perovskite, we conclude that the energetic alignment is equally important and even small changes in the thickness of HTL can have an adverse effect on the *jV* parameters. We successfully demonstrated the robust deposition technique for the HTLs in a fully textured tandem architecture to enable around 30% stabilized PCE tandem devices, which can be further improved to 31.7% by reducing the effective resistance losses and losses due to the energetic mismatch between perovskite/charge transport layer interfaces. The thermal evaporation of HTLs also enables high efficiency ($\sim$26%) tandem cells on large areas with narrow distribution in the *jV* parameters and offers a scalable option for the deposition of HTLs and hence a step closer towards commercialization of the perovskite silicon tandem technology.

Author contributions

B. P. K. conceived the idea, planned, designed and carried out most of the experiments (fabrication of solar cell devices, *jV* measurements, PLQY measurements, BB-XRD, GI-XRD measurements), and prepared the first draft of manuscript. O. E. performed the trPL, contact angle and PESA measurements. O. F. performed *Suns*-V_{OC} and *Suns*-PLI measurements and evaluated the data. A. C performed AFM measurements and evaluated the data. M. B. provided silicon bottom solar cells and provided deep insight in the tandem solar cell data understanding. S. W. provided the facility for PESA measurements. O. S. W., P. S. C. S, S. W. G., and J. B. provided the funding (PrEsto, MaNiTU, KATANA, and Liverpool) as well as deep insight in the understanding of characterization data. All authors reviewed the manuscript and repeatedly helped with manuscript reviews.

Data availability

The data supporting this article have been included as part of the ESI.†

Conflicts of interest

There are no conflicts to declare.

Acknowledgements

This work was funded by the German Federal Ministry for Economic Affairs and Climate Action under Contract No. 03EE1086A (PrEsto) as well as 03EE1087A, 03EE1087B (KATANA), 03EE1189 (Liverpool) and Fraunhofer LIGHTHOUSE PROJECT MaNiTU. We would like to thank J. Zielonka for her support with SEM measurements, K. Aborov and A. Gonzalez Abad for the support with EQE measurements, J. Shaji for the UV-Vis measurements, M. Hanser for the Ellipsometry measurements, K. Zimmermann and H. Nagel with silicon bottom solar cell processing, K. Fischer and J. Myers for technical support. Adrian Callies gratefully acknowledges scholarship support from the Deutsche Bundesstiftung Umwelt (DBU) 20021/728-242.

References

1 S. Mariotti, E. Köhnen, F. Scheler, K. Sveinbjörnsson, L. Zimmermann, M. Piot, F. Yang, B. Li, J. Warby, A. Musiienko, D. Menzel, F. Lang, S. Keßler, I. Levine, D. Mantione, A. Al-Ashouri, M. S. Härtel, K. Xu, A. Cruz, J. Kurpiers, P. Wagner, H. Köbler, J. Li, A. Magomedov, D. Mecerreyes, E. Unger, A. Abate, M. Stolterfoht, B. Stannowski, R. Schlatmann, L. Korte and S. Albrecht, *Science*, 2023, **381**, 63.
2 E. Aydin, E. Ugur, B. K. Yildirim, T. G. Allen, P. Dally, A. Razzaq, F. Cao, L. Xu, B. Vishal, A. Yazmaciyan, A. A. Said, S. Zhumagali, R. Azmi, M. Babics, A. Fell, C. Xiao and S. de Wolf, *Nature*, 2023, **623**, 732.
3 M. H. Futscher and B. Ehrler, *ACS Energy Lett.*, 2016, **1**, 863.
4 X. Y. Chin, D. Turkay, J. A. Steele, S. Tabean, S. Eswara, M. Mensi, P. Fiala, C. M. Wolff, A. Paracchino, K. Artuk, D. Jacobs, Q. Guesnay, F. Sahli, G. Andreatta, M. Boccard, Q. Jeangros and C. Ballif, *Science*, 2023, **381**, 59.
5 NREL, *Best research-cell efficiency chart, Photovoltaic Research*, **https://www.nrel.gov/pv/cell-efficiency.html**.
6 J. Liu, Y. He, L. Ding, H. Zhang, Q. Li, L. Jia, J. Yu, T. W. Lau, M. Li, Y. Qin, X. Gu, F. Zhang, Q. Li, Y. Yang, S. Zhao, X. Wu, J. Liu, T. Liu, Y. Gao, Y. Wang, X. Dong, H. Chen, P. Li, T. Zhou, M. Yang, X. Ru, F. Peng, S. Yin, M. Qu, D. Zhao, Z. Zhao, M. Li, P. Guo, H. Yan, C. Xiao, P. Xiao, J. Yin, X. Zhang, Z. Li, B. He and X. Xu, *Nature*, 2024, **635**, 596–603.
7 J. Liu, M. de Bastiani, E. Aydin, G. T. Harrison, Y. Gao, R. R. Pradhan, M. K. Eswaran, M. Mandal, W. Yan, A. Seitkhan, M. Babics, A. S. Subbiah, E. Ugur, F. Xu, L. Xu, M. Wang, A. U. Rehman, A. Razzaq, J. Kang, R. Azmi, A. A. Said, F. H. Isikgor, T. G. Allen, D. Andrienko, U. Schwingenschlögl, F. Laquai and S. de Wolf, *Science*, 2022, **377**, 302.
8 P. Tockhorn, J. Sutter, A. Cruz, P. Wagner, K. Jäger, D. Yoo, F. Lang, M. Grischek, B. Li, J. Li, O. Shargaieva, E. Unger,

A. Al-Ashouri, E. Köhnen, M. Stolterfoht, D. Neher, R. Schlatmann, B. Rech, B. Stannowski, S. Albrecht and C. Becker, *Nat. Nanotechnol.*, 2022, **17**, 1214–1221.
9 P. Campbell and M. A. Green, *J. Appl. Phys.*, 1987, **62**, 243.
10 J. Lehr, M. Langenhorst, R. Schmager, S. Kirner, U. Lemmer, B. S. Richards, C. Case and U. W. Paetzold, *Sustainable Energy Fuels*, 2018, **8**, 506.
11 F. Gota, R. Schmager, A. Farag and U. W. Paetzold, *Opt. Express*, 2022, **30**, 14172.
12 F. Sahli, J. Werner, B. A. Kamino, M. Bräuninger, R. Monnard, B. Paviet-Salomon, L. Barraud, L. Ding, J. J. Diaz Leon, D. Sacchetto, G. Cattaneo, M. Despeisse, M. Boccard, S. Nicolay, Q. Jeangros, B. Niesen and C. Ballif, *Nat. Mater.*, 2018, **17**, 820.
13 K. Yoshikawa, H. Kawasaki, W. Yoshida, T. Irie, K. Konishi, K. Nakano, T. Uto, D. Adachi, M. Kanematsu, H. Uzu and K. Yamamoto, *Nat. Energy*, 2017, **2**, 17032.
14 D. A. Jacobs, M. Langenhorst, F. Sahli, B. S. Richards, T. P. White, C. Ballif, K. R. Catchpole and U. W. Paetzold, *J. Phys. Chem. Lett.*, 2019, **10**, 3159.
15 Q. Wang, C.-C. Chueh, M. Eslamian and A. K.-Y. Jen, *ACS Appl. Mater. Interfaces*, 2016, **8**, 32068.
16 X. Yan, J. Zheng, L. Zheng, G. Lin, H. Lin, G. Chen, B. Du and F. Zhang, *Mater. Res. Bull.*, 2018, **103**, 150.
17 S. Sajid, A. M. Elseman, H. Huang, J. Ji, S. Dou, H. Jiang, X. Liu, D. Wei, P. Cui and M. Li, *Nano Energy*, 2018, **51**, 408.
18 J. Dai, J. Xiong, N. Liu, Z. He, Y. Zhang, S. Zhan, B. Fan, W. Liu, X. Huang, X. Hu, D. Wang, Y. Huang, Z. Zhang and J. Zhang, *Chem. Eng. J.*, 2023, **453**, 139988.
19 M. Sendner, J. Trollmann and A. Pucci, *Org. Electron.*, 2014, **15**, 2959.
20 Y. Wang, L. Duan, M. Zhang, Z. Hameiri, X. Liu, Y. Bai and X. Hao, *Sol. RRL*, 2022, **6**, 2200234.
21 Y. Kim, E. H. Jung, G. Kim, D. Kim, B. J. Kim and J. Seo, *Adv. Energy Mater.*, 2018, **8**, 1801668.
22 J. C. Yu, J. A. Hong, E. D. Jung, B. Da Kim, S.-M. Baek, S. Lee, S. Cho, S. S. Park, K. J. Choi and M. H. Song, *Sci. Rep.*, 2018, **8**, 1070.
23 K. M. Reza, A. Gurung, B. Bahrami, S. Mabrouk, H. Elbohy, R. Pathak, K. Chen, A. H. Chowdhury, M. T. Rahman, S. Letourneau, H.-C. Yang, G. Saianand, J. W. Elam, S. B. Darling and Q. Qiao, *J. Energy Chem.*, 2020, **44**, 41.
24 W.-Y. Chen, L.-L. Deng, S.-M. Dai, X. Wang, C.-B. Tian, X.-X. Zhan, S.-Y. Xie, R.-B. Huang and L.-S. Zheng, *J. Mater. Chem. A*, 2015, **3**, 19353.
25 L. Mao, T. Yang, H. Zhang, J. Shi, Y. Hu, P. Zeng, F. Li, J. Gong, X. Fang, Y. Sun, X. Liu, J. Du, A. Han, L. Zhang, W. Liu, F. Meng, X. Cui, Z. Liu and M. Liu, *Adv. Mater.*, 2022, **34**, 2206193.
26 S. Zhumagali, F. H. Isikgor, P. Maity, J. Yin, E. Ugur, M. de Bastiani, A. S. Subbiah, A. J. Mirabelli, R. Azmi, G. T. Harrison, J. Troughton, E. Aydin, J. Liu, T. Allen, A. U. Rehman, D. Baran, O. F. Mohammed and S. de Wolf, *Adv. Energy Mater.*, 2021, **11**, 2101662.
27 G. Li, Y. Jiang, S. Deng, A. Tam, P. Xu, M. Wong and H.-S. Kwok, *Adv. Sci.*, 2017, **4**, 1700463.
28 A. Farag, P. Fassl, H. Hu, T. Feeney, A. Quintilla, M. A. Ruiz-Preciado, W. Hempel, D. Bagrowski, P. Noack, B. Wattenberg, T. Dippell and U. W. Paetzold, *Adv. Funct. Mater.*, 2023, **33**, 2210758.
29 I. Kafedjiska, I. Levine, A. Musiienko, N. Maticiuc, T. Bertram, A. Al-Ashouri, C. A. Kaufmann, S. Albrecht, R. Schlatmann and I. Lauermann, *Adv. Funct. Mater.*, 2023, **33**, 2302924.
30 A. Al-Ashouri, A. Magomedov, M. Roß, M. Jošt, M. Talaikis, G. Chistiakova, T. Bertram, J. A. Márquez, E. Köhnen, E. Kasparavičius, S. Levcenco, L. Gil-Escrig, C. J. Hages, R. Schlatmann, B. Rech, T. Malinauskas, T. Unold, C. A. Kaufmann, L. Korte, G. Niaura, V. Getautis and S. Albrecht, *Energy Environ. Sci.*, 2019, **12**, 3356.
31 P. S. C. Schulze, K. Wienands, A. J. Bett, S. Rafizadeh, L. E. Mundt, L. Cojocaru, M. Hermle, S. W. Glunz, H. Hillebrecht and J. C. Goldschmidt, *Thin Solid Films*, 2020, **704**, 137970.
32 S. Yu, Z. Xiong, H. Zhou, Q. Zhang, Z. Wang, F. Ma, Z. Qu, Y. Zhao, X. Chu, X. Zhang and J. You, *Science*, 2023, **382**, 1399.
33 N. Phung, M. Verheijen, A. Todinova, K. Datta, M. Verhage, A. Al-Ashouri, H. Köbler, X. Li, A. Abate, S. Albrecht and M. Creatore, *ACS Appl. Mater. Interfaces*, 2022, **14**, 2166.
34 M. Wu, X. Li, Z. Ying, Y. Chen, X. Wang, M. Zhang, S. Su, X. Guo, J. Sun, C. Shou, X. Yang and J. Ye, *Adv. Funct. Mater.*, 2023, **33**, 2304708.
35 S. Kralj, P. Dally, P. Bampoulis, B. Vishal, S. de Wolf and M. Morales-Masis, *ACS Mater. Lett.*, 2024, **6**, 366.
36 S. M. Park, M. Wei, N. Lempesis, W. Yu, T. Hossain, L. Agosta, V. Carnevali, H. R. Atapattu, P. Serles, F. T. Eickemeyer, H. Shin, M. Vafaie, D. Choi, K. Darabi, E. D. Jung, Y. Yang, B. Da Kim, S. M. Zakeeruddin, B. Chen, A. Amassian, T. Filleter, M. G. Kanatzidis, K. R. Graham, L. Xiao, U. Rothlisberger, M. Grätzel and E. H. Sargent, *Nature*, 2023, **624**, 289.
37 M. Pitaro, J. S. Alonso, L. Di Mario, D. Garcia Romero, K. Tran, T. Zaharia, M. B. Johansson, E. M. J. Johansson and M. A. Loi, *J. Mater. Chem. A*, 2023, **11**, 11755.
38 A. Farag, T. Feeney, I. M. Hossain, F. Schackmar, P. Fassl, K. Küster, R. Bäuerle, M. A. Ruiz-Preciado, M. Hentschel, D. B. Ritzer, A. Diercks, Y. Li, B. A. Nejand, F. Laufer, R. Singh, U. Starke and U. W. Paetzold, *Adv. Energy Mater.*, 2023, **13**, 2203982.
39 E. Aydin, J. Liu, E. Ugur, R. Azmi, G. T. Harrison, Y. Hou, B. Chen, S. Zhumagali, M. de Bastiani, M. Wang, W. Raja, T. G. Allen, A. U. Rehman, A. S. Subbiah, M. Babics, A. Babayigit, F. H. Isikgor, K. Wang, E. van Kerschaver, L. Tsetseris, E. H. Sargent, F. Laquai and S. de Wolf, *Energy Environ. Sci.*, 2021, **14**, 4377.
40 I. Susic, K. P. S. Zanoni, A. Paliwal, I. C. Kaya, Z. Hawash, M. Sessolo, E. Moons and H. J. Bolink, *Sol. RRL*, 2022, **6**, 2100882.
41 O. Er-raji, M. A. Mahmoud, O. Fischer, A. J. Ramadan, D. Bogachuk, A. Reinholdt, A. Schmitt, B. P. Kore, T. W. Gries, A. Musiienko, O. Schultz-Wittmann, M. Bivour,

M. Hermle, M. C. Schubert, J. Borchert, S. W. Glunz and P. S. Schulze, *Joule*, 2024, **8**, 1.

42 O. Er-raji, A. J. Bett, S. Lange, H. Nagel, M. Bivour, O. Schultz-Wittmann, C. Hagendorf, M. Hermle, J. Borchert, S. W. Glunz and P. S. C. Schulze, *Prog. Photovoltaics*, 2023, 1–14.

43 C. Bi, Q. Wang, Y. Shao, Y. Yuan, Z. Xiao and J. Huang, *Nat. Commun.*, 2015, **6**, 7747.

44 P. Caprioglio, C. M. Wolff, O. J. Sandberg, A. Armin, B. Rech, S. Albrecht, D. Neher and M. Stolterfoht, *Adv. Energy Mater.*, 2020, **10**, 2000502.

45 V. J.-Y. Lim, A. J. Knight, R. D. J. Oliver, H. J. Snaith, M. B. Johnston and L. M. Herz, *Adv. Funct. Mater.*, 2022, **32**, 2204825.

46 A. Al-Ashouri, E. Köhnen, B. Li, A. Magomedov, H. Hempel, P. Caprioglio, J. A. Márquez, A. B. Morales Vilches, E. Kasparavicius, J. A. Smith, N. Phung, D. Menzel, M. Grischek, L. Kegelmann, D. Skroblin, C. Gollwitzer, T. Malinauskas, M. Jošt, G. Matič, B. Rech, R. Schlatmann, M. Topič, L. Korte, A. Abate, B. Stannowski, D. Neher, M. Stolterfoht, T. Unold, V. Getautis and S. Albrecht, *Science*, 2020, **370**, 1300.

47 J. Suo, B. Yang, D. Bogachuk, G. Boschloo and A. Hagfeldt, *Adv. Energy Mater*, 2024, 2400205.

48 J. Lee, K. Lee, K. Kim and N.-G. Park, *Sol. RRL*, 2022, **6**, 2200623.

49 C. Momblona, L. Gil-Escrig, E. Bandiello, E. M. Hutter, M. Sessolo, K. Lederer, J. Blochwitz-Nimoth and H. J. Bolink, *Energy Environ. Sci.*, 2016, **9**, 3456.

50 D. Pérez-del-Rey, L. Gil-Escrig, K. P. S. Zanoni, C. Dreessen, M. Sessolo, P. P. Boix and H. J. Bolink, *Chem. Mater.*, 2019, **31**, 6945.

51 L. Krückemeier, U. Rau, M. Stolterfoht and T. Kirchartz, *Adv. Energy Mater.*, 2020, **10**, 1902573.

52 O. Fischer, A. D. Bui, F. Schindler, D. Macdonald, S. W. Glunz, H. T. Nguyen and M. C. Schubert, *Prog. Photovoltaics*, 2023, 1–14.

